NANO · MICRO small
www.small-journal.com

Soft Synthetic Cells with Mobile Membrane Ligands for Ex Vivo Expansion of Therapy-Relevant T Cell Phenotypes

*Anna Burgstaller, Nils Piernitzki, Nadja Küchler, Marcus Koch, Thomas Kister, Hermann Eichler, Tobias Kraus, Eva C. Schwarz, Michael L. Dustin, Franziska Lautenschläger, and Oskar Staufer**

The expansion of T cells ex vivo is crucial for effective immunotherapy but currently limited by a lack of expansion approaches that closely mimic in vivo T cell activation. Taking inspiration from bottom-up synthetic biology, a new synthetic cell technology is introduced based on dispersed liquid-liquid phase-separated droplet-supported lipid bilayers (dsLBs) with tunable biochemical and biophysical characteristics, as artificial antigen presenting cells (aAPCs) for ex vivo T cell expansion. These findings obtained with the dsLB technology reveal three key insights: first, introducing laterally mobile stimulatory ligands on soft aAPCs promotes expansion of IL-4/IL-10 secreting regulatory CD8$^+$ T cells, with a PD-1 negative phenotype, less prone to immune suppression. Second, it is demonstrated that lateral ligand mobility can mask differential T cell activation observed on substrates of varying stiffness. Third, dsLBs are applied to reveal a mechanosensitive component in bispecific Her2/CD3 T cell engager-mediated T cell activation. Based on these three insights, lateral ligand mobility, alongside receptor- and mechanosignaling, is proposed to be considered as a third crucial dimension for the design of ex vivo T cell expansion technologies.

1. Introduction

Activation of T cells is a fundamental physiological process for immunity. It is also a critical initial step for the ex vivo expansion of T cells that are applied for adoptive T cell transfer in cancer immunotherapy.[1] One of the current challenges that limit a wider application of such immunotherapeutic approaches is the reliable expansion of T cells with suitable phenotypes from a small patient-derived starting population of immune cells. Although this poses a significant challenge, it also presents an opportunity to explore the practical application of emerging bioengineering concepts, such as bottom-up synthetic biology and engineering natural cell-synthetic cell interfaces. Specifically, the challenge lays in the need to expand T cells in a phenotypic state compatible with effective therapies, e.g. non-exhausted cells

A. Burgstaller, N. Piernitzki, M. Koch, T. Kister, T. Kraus, O. Staufer
INM – Leibniz Institute for New Materials
Campus D2 2, 66123 Saarbrücken, Germany
E-mail: oskar.staufer@leibniz-inm.de

A. Burgstaller, N. Piernitzki, O. Staufer
Helmholtz Institute for Pharmaceutical Research Saarland
Helmholtz Center for Infection Research
Campus E8 1, 66123 Saarbrücken, Germany

A. Burgstaller, N. Piernitzki, F. Lautenschläger, O. Staufer
Center for Biophysics
Saarland University
Campus Saarland, 66123 Saarbrücken, Germany

N. Küchler, E. C. Schwarz
Biophysics, Center for Integrative Physiology and Molecular Medicine (CIPMM)
School of Medicine, Saarland University
Building 48, 66421 Homburg, Germany

H. Eichler
Institute of Clinical Hemostaseology and Transfusion Medicine
Saarland University and Saarland University Medical Center
Homburg Germany

T. Kraus
Saarland University, Colloid and Interface Chemistry
66123 Saarbrücken, Germany

M. L. Dustin, O. Staufer
Kennedy Institute of Rheumatology, Nuffield Department of Orthopedics, Rheumatology and, Musculoskeletal Sciences
University of Oxford
Oxford UK

F. Lautenschläger
Experimental Physics, Faculty of Natural Science and Technology
Saarland University
Campus Saarbrücken, 66123 Saarbrücken, Germany

O. Staufer
Max Planck Bristol Centre for Minimal Biology
Cantock's Close, Bristol BS8 1TS, UK

The ORCID identification number(s) for the author(s) of this article can be found under https://doi.org/10.1002/smll.202401844

DOI: 10.1002/smll.202401844

with increased resistance against immunosuppression, memory-formation, regulatory functions and effector potency.[2] Fine-tuning the phenotypic composition of the expanded T cell populations is also a crucial requirement to tailor T cell products to the specific needs of different immunotherapeutic approaches (TCR transduced T cells, chimeric antigen receptor T cells or reinfused tumor infiltrating lymphocytes[3]). With the use of antibody-decorated polystyrene-based beads (e.g., Dynabeads or MACSiBead) that cross-link and activate CD3, CD2 or CD28 receptors on T cell membranes, the simple expansion of T cells ex vivo has become a routine procedure.[4] Effectively, such dispersed beads mimic in vivo signaling by antigen presenting cells (APCs) and provide a controlled and reproducible technology for generating large numbers of T cells by means of biomimetic artificial APCs (aAPCs).[5] Particularly, the application of dispersed aAPC particles presents advantages in comparison to antibody functionalized surfaces, such as hydrogels or solid supports, due to their compatibility with 3D cultures and their facile upscaling to therapeutic and industrial-scale production systems.

However, while cell-mimicking solid antibody-decorated beads are able to initiate crucial events in T cell signaling, like T cell receptor triggering and co-stimulation (signal I and II during T cell activation),[6] they fail to provide key biophysical cues of APCs that direct and fine-tune the T cell expansion and differentiation process in vivo.[5,7] Biophysical characteristics that aAPCs need to emulate to reach more programmable T cell expansion include cell stiffness, density of ligands, size, surface topography, and notably, lateral mobility of ligands on a membrane. In this biophysical context, several studies highlight the importance of mechanosensation for T cell stimulation and the role of aAPCs stiffness for successful T cell activation.[8] Increased IL-2 production from mouse $CD4^+$ T cells has been correlated with increasing stiffness of a stimulating polyacrylamide hydrogel.[9] On the other hand, a reverse trend has been observed for polydimethylsiloxane (PDMS)-based substrates and human $CD4^+$ T cells.[10] A more recent study suggests that these two seemingly conflicting trends could be inherently interconnected and represent a biphasic mechanosensitive response.[11] Of note, mechanosensation has also been demonstrated in other immune cells, such as NK cells, where dispersed alginate particles substrates with varying stiffnesses have been applied to assess mechanotransduction.[12] These studies demonstrate that stiffness plays a critical role in modulating essential aspects of T cell activation and differentiation, underscoring the need for advanced aAPC technologies that effectively cover a broader range of tissue stiffnesses, which lay between 1 kPa (lymphatic tissue) to some hundred kPa (solid tumors).[13,14]

Arguably of greater significance then stiffness-related effects, previous aAPC approaches have relied on immobilized and adsorbed ligands on solid, elastomer or hydrogel supports, which fail to emulate the dynamic mobile lipid membrane environment and membrane-membrane interface present in the in vivo scenario. Specifically, the lateral mobility and spatial segregation of receptors and ligands have been identified as critical factors for the formation of immune synapse (IS) architectures at the APC-T cell interface.[15,16] ISs are central regulatory structures that orchestrate initial signaling events during T cell expansion. Regulatory ligands and co-receptors such as PD-1, CD58, CTLA-4, CD28 or ICAM1 distinctly and spatially segregate into supramolecular clusters, regulatory contact zones and receptor microclusters that are essential for accurate antigen recognition, regulation of downstream signaling and prevention of unregulated interactions for controlled T cell activation.[17] Importantly, accurate IS assembly largely relies on lateral ligand mobility to enable formation of the spatially segregated zones by APCs that direct T cell activation. To achieve comparable levels of biophysical fine tuning in aAPCs, it is necessary to engineer and implement this "membrane context" and the associated ligand mobility into particles, as such factors play a crucial role in emulating the in vivo scenario and improving the efficiency and specificity of T cell activation.

With recent advancements in bottom-up synthetic biology, numerous new techniques have emerged to construct artificial replicas of living cells that allow for the analysis of fundamental processes of life under defined conditions.[18–20] These synthetic cell technologies also have immense potential for translation into advanced applications in biomedicine, as they accurate mimic structural and functional features of living cells.[21] In principle, they could be applied to build biomimetic systems that act as aAPCs, offering potential advantages due to the increased cell-like characteristics.[22] Intriguingly, since compartmentalization is a key characteristic of life, a great amount of work in the field of bottom-up synthetic biology has focused on engineering well-controlled membrane systems.[23] This is a specific advantage when attempting to construct aAPCs, since their design necessitates a faithful emulation of the cellular membrane interface.[24] One of the most widely applied techniques for synthetic cell assembly involves the use of oil-in-water or water-in-oil droplet-templating approaches.[25] Such systems not only enable high-throughput production, but also offer finely adjustable production parameters and a wide range of molecular configurations to adjust biophysical characteristics such as stiffness, membrane composition, size, and bioactive content. Moreover, as liquid droplet templating approaches are based on fully viscous oils, they potentially allow to produce ultra-soft dispersed substrates for T cell expansion. In this context, previous studies have highlighted the use of elastomers, such as PDMS, for the activation of T cells due to their low cost and high biocompatibility.[10] Additionally, it has been demonstrated that phospholipid bilayers can be deposited on cross-linked solid 2D PDMS substrates, allowing for IS formation and spatial ligand seggregation.[26,27] Therefore, implementing an oil elastomer-based bottom-up synthetic cell assembly approach may present innovative avenues for engineering aAPC systems that better emulate the lipid membrane of natural APCs and integrate additional biophysical cues.

Inspired by bottom-up synthetic biology approaches, we designed a droplet supported lipid bilayer (dsLB) synthetic cell technology that integrates mobile lipid membrane bilayers and tunable ligand densities in combination with adjustable substrate stiffnesses as a novel aAPC technology. DsLBs are based on micrometer-sized oil droplets generated through oil-in-water emulsions and coated with protein-functionalized phospholipid bilayer membranes. We demonstrate the application of dsLBs for the activation of primary human CD8+ T cells in vitro, benchmarked to the commerically available DynaBead technology, and show that the resulting T cell populations are composed of a regulatory- and memory-like phenotype. By adding lateral membrane fluidity in the dsLB systems we enable an additional layer

of control, largely neglected by previous technologies, to fine-tune the ex vivo expansion of T cells in therapeutic quantities.

2. Results

We designed a synthetic cell assembly strategy for dsLBs based on charge-mediated lipid bilayer coating of PDMS oil microdroplets (**Figure** 1A). For this, liquid-liquid phase separated oil-in-water (o/w) droplets are produced from PDMS/PBS emulsions and stabilized by anionic sodium dodecyl sulfate (SDS) surfactants. After addition of Mg^{2+} divalent cations, net-negatively charged small unilamellar vesicles (SUVs), containing fluorescent (Rhodamin B or Atto488) and nitrilotriacetic acid-Ni^{2+} (NTA-(Ni^{2+}))-functionalized lipid head groups, are deposited on the droplets surfaces to form unilamellar droplet supported lipid bilayers. We anticipated that this fabrication process, performed under physiological buffer conditions, would offer scalable batch production of biocompatible droplets with spherical lipid membrane surface and low viscosity oil core. This allows to produce soft dispersed aAPC substrates (≈1 kPa) for T cell activation, and further to cross-link the dsLB oil core to gradually increase their stiffness into the MPa range, analogous to bulk PDMS substrates.

2.1. Droplet Supported Lipid Bilayer Formation and Characterization

In a first step, we produced PDMS-based o/w emulsion (1:10 w/w ratio) by sonication and formed dsLBs according to the designed formation strategy. Inspection of the dsLB solutions by environmental scanning electron microscopy (ESEM) revealed stable spherical droplets with smooth surface topography and similar contrast characteristics between the individual droplets (Figure 1B,C). Furthermore, no fusion of droplets was observed, even at extremely high, almost spherical packing densities, demonstrating their stability. Confocal microscopy imaging of the assembled dsLBs showed a fluorescent lipid layer surrounding the droplets, consistent with our assembly blueprint (Figure 1D). Of note, similar droplet structures could be assembled with a variety of other silicon oils (Figure S1, Supporting Information). Toward assessing the importance of charge-based interactions for dsLB assembly, we replaced the ionic surfactant SDS with the non-ionic surfactant Triton X-100 and found no encircling fluorescent lipid layer on the droplet surface indicating unsuccessful dsLB assembly (Figure S2A, Supporting Information). Similar results were obtained when attempting to form dsLBs without Mg^{2+} ions (Figure S2B, Supporting Information), resulting in droplets without surrounding lipid layer. We further performed dynamic light scattering measurements of dsLB zeta potentials at the different assembly stages to assess the assumed charge-mediated formation mechanism (Figure 1E). While "naked" PDMS droplets stabilized by anionic SDS show a large negative zeta potential of −57 mV (± 6 mV), addition of $MgCl_2$ reduced the zeta potential to -45 mV (±1 mV). Subsequent incubation with SUVs further reduced the dsLB zeta potential to −26 mV (±1 mV), which is comparable to the value measured for the SUVs used for dsLB assembly (−19 mV (±3 mV)). Taken together, this indicates a sequential layer-by-layer assembly process of lipid membranes on oil droplet supports, driven by charge-mediated interactions between the individual building blocks.

Toward optimizing the dsLB formation process as well as size distribution, we varied the SDS and $MgCl_2$ concentration used for production between 0.1 and 10 mM as well as 10 and 100 mM, respectively (Figure S3, Supporting Information). We found that the optimal combination of dsLB size, lipid layer intensity and droplet quantity could be achieved at 1 mM SDS and 20 mM $MgCl_2$. Moreover, these conditions resulted in a median dsLB size of 3.75 µm (±2.61 µm), a suitable range for T cell activation,[28] and a PDI of 0.58. Only SDS concentrations below 1 mM and $MgCl_2$ concentrations above 20 mM resulted in abnormal droplet morphologies, with thick fluorescent lipid layers. Therefore, the formation process of dsLBs appears to be highly resilient across a broader range of SDS and $MgCl_2$ concentrations, supporting that dsLB assembly is primarily driven by charge-based interactions, which confer robustness to the process. Of note, varying the SUV concentration added in the final formation step did not significantly impact on the size distribution of the dsLBs nor the production yield (Figure S4, Supporting Information). Additionally, we evaluated the storage stability of dsLBs in phosphate-buffered saline at 4 °C over a duration of 75 days to estimate the shelf life of the particles (Figure S5, Supporting Information). Confocal microscopy analysis showed that the morphology, size, and lipid layer fluorescence of the dsLBs remained unaltered throughout the experimental period, suggesting that the dsLBs are highly stable in solution. Based on this optimization, we defined 1 mM SDS and 20 mM $MgCl_2$ as the standard condition for dsLB formation further applied throughout our study.

The results obtained from confocal microscopy imaging demonstrated the presence of an encircling lipid layer on the oil droplet core. However, it was not possible to deduce information on the configuration of the lipid leaflets from this, and specifically, to exclude the formation of a monolayer with lipid fatty-acid tails extending into the oil core, as previously reported for other biomimetic droplet systems.[29] To demonstrate the presence of a lipid bilayer on the surface of the dsLBs, we performed previously developed nitrobenzoxadiazole (NBD) quenching assays using lipids with NBD fluorophore-conjugated head groups (Figure 1F).[30] In brief, this assay uses the oxyanion dithionite, which effectively quenches NBD fluorescence but is impermeable to lipid bilayers. Upon addition of dithionite to lipid bilayer membranes containing NBD fluorescent headgroups, such as SUVs or presumably dsLBs, half of the NBD fluorescence is quenched, reflecting the equal distribution of NBD fluorophores between the leaflets. Consequently, complete loss of fluorescence signal occurs in the presence of a lipid monolayer, whereas only a fraction of the initial fluorescence is lost if multilayer membranes exist. As this assay is sensitive to the ratio of NBD fluorophores and dithionite molecules, we quantified NBD fluorescence of dsLBs in a dithionite dilution series between 0.2 and 50 mM (Figure 1G). We found a plateau area between 6.25 and 50.0 mM dithionite where dsLB fluorescence was quenched to ≈50% of the original fluorescence level. This quantitative analysis strongly indicates the presence of a lipid bilayer on dsLBs. A finding that not only aligns with the charge-based formation model but that is further supported by cryogenic transmission electron microscopy (cryoTEM) analysis of the dsLBs (Figure S6,

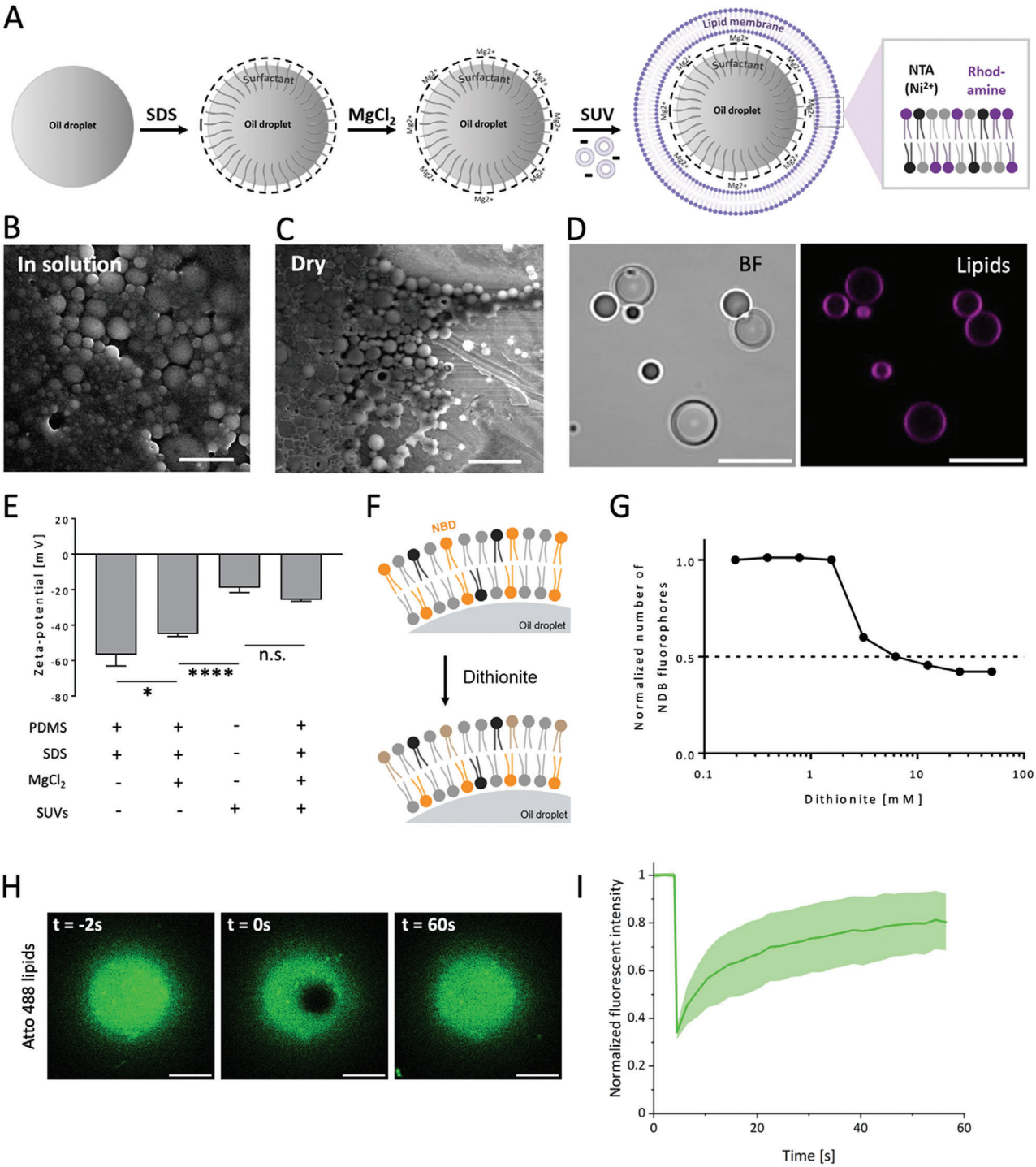

Figure 1. Oil droplet supported lipid bilayer assembly. A) Schematic illustration of the charge-mediated bilayer assembly on PDMS oil droplets. Droplets are stabilized by anionic surfactants that bind divalent Mg^{2+} cations for deposition of an anionic lipid bilayer with fluorescent and NTA-functionalized lipids. B and C) Representative environmental scanning electron microscopy micrographs of PDMS droplets in phosphate buffered saline (B) and in dried state (C). Scale bars are 10 µm in B and 20 µm in C. D) Representative confocal microscopy and bright field images of the lipid layer formed around the oil droplets. Scale bars are 10 µm. E) Dynamic light scattering analysis of the dsLB zeta potential at the different assembly stages indicated in A. Results are shown as mean ±SD from n = three measurement replicates. $^{*}p < 0.05$, $^{****}p < 0.001$, one-way ANOVA. F) Schematic illustration of NBD fluorescence quenching by dithionite in lipid bilayers. Membrane impermeable dithionite only quenches fluorophores in the outer membrane leaflet resulting in an intensity decrease of 50%. G) Fluorescence intensity quantification of dsLBs with NBD containing lipid membranes in a dithionite dilution series. Results shown as mean from n=2 technical replicates. H) Representative pre-bleach, post-bleach and recovered confocal microscopy images of a FRAP experiment on dsLBs. Scale bars are 5 µm. I) Fluorescence recovery quantification of FRAP series on dsLBs. Line indicates mean from n = 9 dsLBs, shaded green indicates standard deviation.

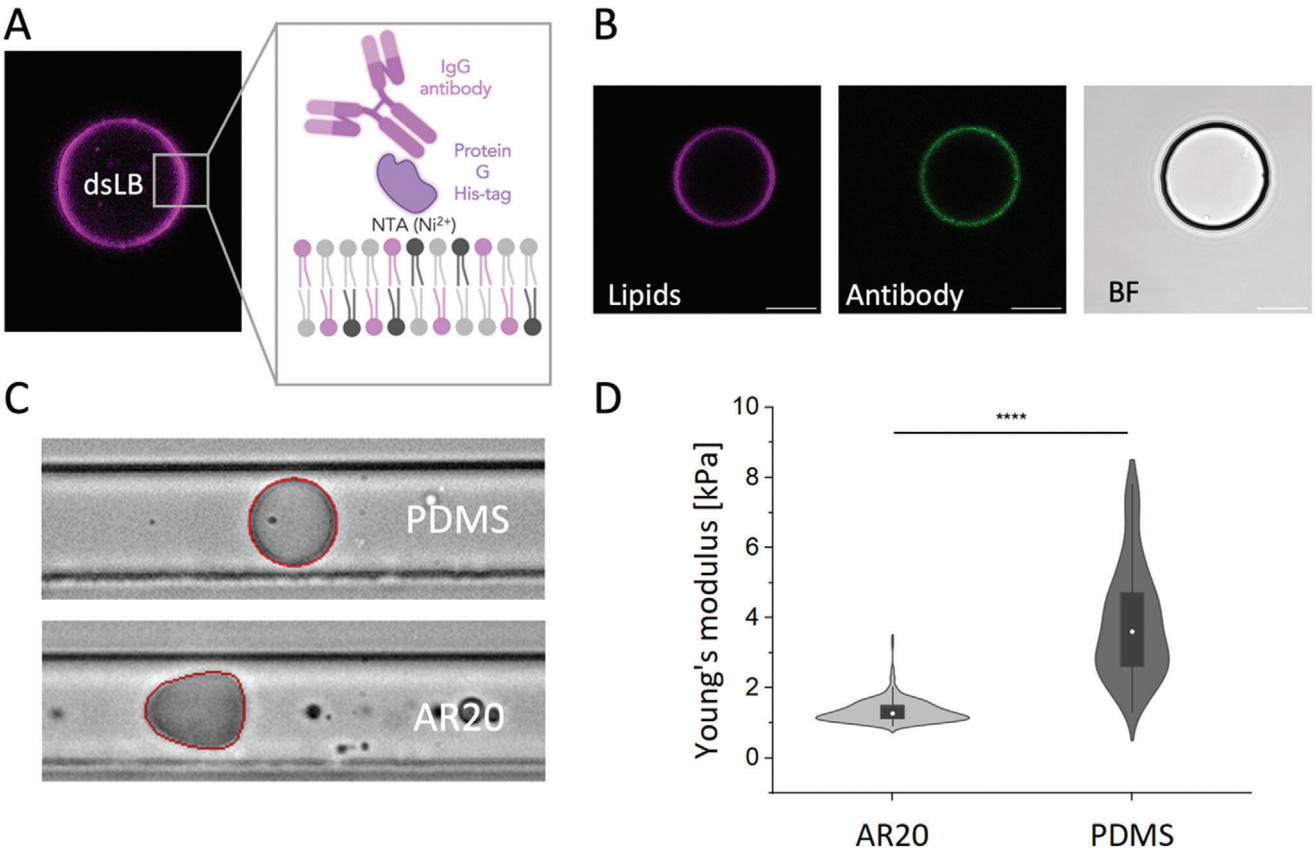

Figure 2. DsLB functionalization with recombinant proteins and antibodies. A) Schematic illustration of dsLB functionalization with IgG antibodies via histidine-tagged protein G coupled to NTA(Ni^{2+}) lipids in the dsLB membrane. B) Representative confocal microscopy and bright field images of the dsLB lipid layer (magenta) decorated with anti-CD3 AlexaFluor488 (green). Scale bars are 10 µm. C) Representative bright field images of dsLBs formed from PDMS (top) and AR20 (bottom) silicon oils within RT-DC channels under deformation. D) RT-DC quantification of dsLB Young´s modulus for droplets formed from PDMS and AR20 oil. Results shown as median and 0.25–0.75 quartiles from n > 70 single droplets. $^{****}p < 0.001$, unpaired two-tailed student t test.

Supporting Information). While our attempts to form vitreous ice layers around the dsLBs for cryoTEM analysis were unsuccessful, we were able to resolve membrane-like structures on the dsLBs that were similar in thickness to the SUVs used for their assembly. Moreover, fluorescence recovery after photobleaching (FRAP) analysis demonstrated the lateral mobility of the lipids on the dsLB surface (Figure 1H,I). We measured half recovery rates of 12.2 sec (±7.7 sec) and mobile fractions of >0.72 (± 0.15), which is in good agreement with lipid diffusion characteristics in other supported lipid bilayer model systems, specifically on PDMS supports.[27] Taken together, this provides compelling evidence that dsLBs are enveloped by a lipid bilayer membrane and are therefore suitable models of living cell membranes.

2.2. DsLB Functionalization and Stiffness Modulation

Incorporation of NTA(Ni^{2+})-functionalized lipids allowed us to conjugate poly-histidine-tagged recombinant proteins, specifically IgG antibodies, on the dsLB surface (**Figure** 2A,B). We calibrated the quantitative conjugation of adjustable antibody surface densities with fluorescent beads presenting known molecules of equivalent soluble fluorochrome (MESF) (Figure S7A,B, Supporting Information). For this, we produced dsLBs conjugated with recombinant his-tagged protein G to capture AlexaFluor488-coupled antibodies on the dsLB surface (Figure S7C, Supporting Information) and spiked these samples with calibration beads. This is a modular and flexible approach that allows to conjugate different types of stimulatory IgGs on the dsLB surface. Based on confocal imaging of the dsLBs and MESF bead fluorescence, we established calibration curves and derived regression parameters to determine the surface density of antibodies on the dsLBs. This approach allowed us to reliably vary antibody densities in the range of 20 – 200 molecules/ µm^2 (Figure S7D, Supporting Information), which is not only in the range of natural ligand densities found on APCs (typically between 1 and 1000 ligands µm^2) but also of the densities applied in other APC technologies.[31,32] These results also demonstrate that dsLBs can present T cell stimulatory antibodies on their surface, which has proven to be a winning strategy for several other aAPCs that typically use anti-CD3 and anti-CD28 antibodies to trigger initial activation and co-stimulation signals for T cell expansion.

In a next step, we aimed to characterize the elastic properties of the dsLBs. Typically, aAPC technologies apply particles and substrates with elastic moduli of up to ≈2 GPa, such as solid beads. Of note, depending on cross-linking degree, duration and

temperature, the elastic modulus of PDMS elastomers can vary between ≈100 kPa to 3 MPa.[33,34] As dsLBs applied so far are based on non-cured fully-viscose core PDMS droplets, their elastic modulus is expected to be close to 0 kPa, as for any fluid with Newtonian behavior, which implies that the material behaves in a purely viscous manner without storing any elastic energy. However, they still display an elastic component that originates from the considerable surface tension at the oil-water-interface (Video S1, Supporting Information). Therefore, the effective elastic modulus of dsLBs is a product of the oil core elastic properties, which is mainly set by the oil viscosity or by the degree of cross-linking, and the surface tension at the dsLB-water interphase. We measured the apparent elastic modulus of dsLBs in high throughput by real time deformation cytometry (RT-DC) at a single droplet level (Figure 2C). For dsLBs based on PDMS oil with a viscosity of 5100 cP (hereafter referred to as soft dsLBs), we measured an average apparent elastic modulus (E modulus) of 3.85 kPa (±1.60 kPa) (Figure 2D). Interestingly, when forming dsLBs based on the silicon oil AR20, which has a lower viscosity of 200 cP, the effective elastic modulus of the dsLBs could be reduced to 1.34 kPa (±0.32 kPa). Therefore, dsLBs with non-cross linked core exhibit elastic characteristics comparable to the lower range of physiological cell stiffnesses.

Toward increasing the elastic modulus of the dsLBs core, we cross-linked the PDMS after the emulsification but before the addition of $MgCl_2$ and formation of the bilayers. For this, the PDMS droplets were cured in a 10:1 (stiff dsLBs) and 50:1 (firm dsLBs) PDMS to curing agent (CA) ratio. For both stiff and firm dsLBs, we successfully produced droplets, that were even stable in air (**Figure 3**A), and from which dsLBs with the characteristic encircling lipid layer could be assembled (Figure 3B). The cured PDMS bulk material displayed mean elastic moduli of 2990 kPa (±8.94 kPa) and 5.75 kPa (±0.66 kPa) for stiff and firm PDMS bulk material, respectively, as measured by compression rheology (Figure S8, Supporting Information). However, the elastic properties of elastomers on a microscale can differ considerably from their bulk properties. We therefore measured the microscale elastic properties by nano-indentation analysis and found elastic moduli of 4.59 kPa (±0.59 kPa), 11.08 kPa (±2.95 kPa) and 163.46 kPa (±64.33 kPa) for soft, firm and stiff dsLBs, respectively (Figure 3C). Of note, FRAP analysis demonstrated that the dsLB membranes on the cured droplets remained mobile, with mobile fractions of 0.90 (±0.09) and 0.92 (±0.09) as well as half recovery rates of 19.17 s (±6.87 s) and 21.10 sec (±5.57 s) for stiff and firm dsLBs, respectively (Figure 3D,E). These findings illustrate that PDMS cross-linking can produce dsLBs with varying degrees of stiffness, with the core stiffness being adjustable over three orders of magnitude. Remarkably, the dsLBs are able to maintain their membrane fluidity throughout this process. Of note, stiffnesses in the higher kPa range greatly exceed the stiffnes of APCs found in vivo and are generally considered unphysioligical but to have been described to induce differential expansion and activation effects on T cells.[11]

For the development of synthetic cell-based T cell expansion technologies, a crucial practical aspect is the ability to effectively separate the expanded T cells from the aAPCs. This is particularly important for the safe reintroduction of T cells into patients. A common method in bead-based technologies for achieving this separation is magnetic isolation. To seamlessly introduce dsLB in such established workflows, we synthesized iron oxide magnetic nanoparticles (NPs) with diameters of 6.6 nm (±1.4 nm, n = 10 particles, cores measured in electron microscopy) (Figure S9A, Supporting Information). To incorporate these NPs into the hydrophobic dsLB core, we functionalized their surface with poly(dimethylsiloxane) using a ω-(carboxy decyl)-C10 anchor. Bright field microscopy confirmed the successful integration of the NPs into the dsLB core, which could then be magnetically separated from the solution (Figure S9B and Video S2, Supporting Information). Our results indicated that as little as 70 mg mL^{-1} NPs is sufficient for effective dsLB separation from the solution (Figure S9C, Supporting Information). Further transmission electron microscopy-coupled energy dispersive X-ray (EDX) analysis demonstrated disperesed integration of the particles into the oil core (Figure S9D, Supporting Information) and quantification of primary human $CD8^+$ T cell viability after incubation with the magnetic dsLBs over 48 h showed no significant cytotoxic effects.

2.3. T Cell Activation and Expansion by DropletSupported Lipid Bilayers

In order to evaluate the potential of dsLBs to activate T cells for expansion, we conjugated them with anti-CD3 and anti-CD28 (in a 1:4 ratio) at 200 molecules μm^2 and incubated them with human primary $CD8^+$ T cells that were isolated from platelet apheresis kits from voluntary healthy donors by negative selection.[35] After a brief incubation period of only 4 hours, we observed frequent contact formation between the T cells and the dsLBs, resulting in polarized T cell morphologies (**Figure 4**A). Additionally, through the use of fluorescently labeled anti-CD3 antibodies immobilized on the dsLB surface, we found that anti-CD3 accumulates at the side of T cell adhesion, which is indicative for antibody recruitment, IS formation and the lateral mobility of the ligands on the dsLB surface (Figure 4B). Further, after an expansion phase of 4 days, we observed formation of larger cell aggregates, similar to those observed for T cell cultures expanded using the fields´-gold standard: solid polystyrene bead-based anti-CD3/CD28 DynaBeads (Figure 4C). These results suggest that dsLBs can activate T cells through antibody engagement and IS formation, resulting in expansion.

We further quantified the expansion of $CD8^+$ T cells when activated with dsLBs of varying stiffness, comparing these to expansions achieved with anti-CD3/CD28 DynaBeads. Our findings revealed that dsLBs were only slightly less effective, showing a 34-28% lower expansion fold, compared to DynaBeads (Figure 4D). Surprisingly, the stiffness of the dsLBs did not significantly affect the expansion rates. This observation aligns with flow cytometry analyses of the activation marker CD25, which indicated similar $CD25^+$ populations in T cells expanded with dsLBs of varying stiffness (Figure 4E and gating strategy in Figure S10, Supporting Information).

A critical parameter for T cell expansion for immunotherapy is, apart from their phenotype (e.g., memory, effector, regulatory), their susceptibility to immune suppression in the cancer microenvironment. To evaluate the susceptibility of dsLB-expanded T cells to immune suppression, we assessed the expression of the immune checkpoint receptor PD-1, typically

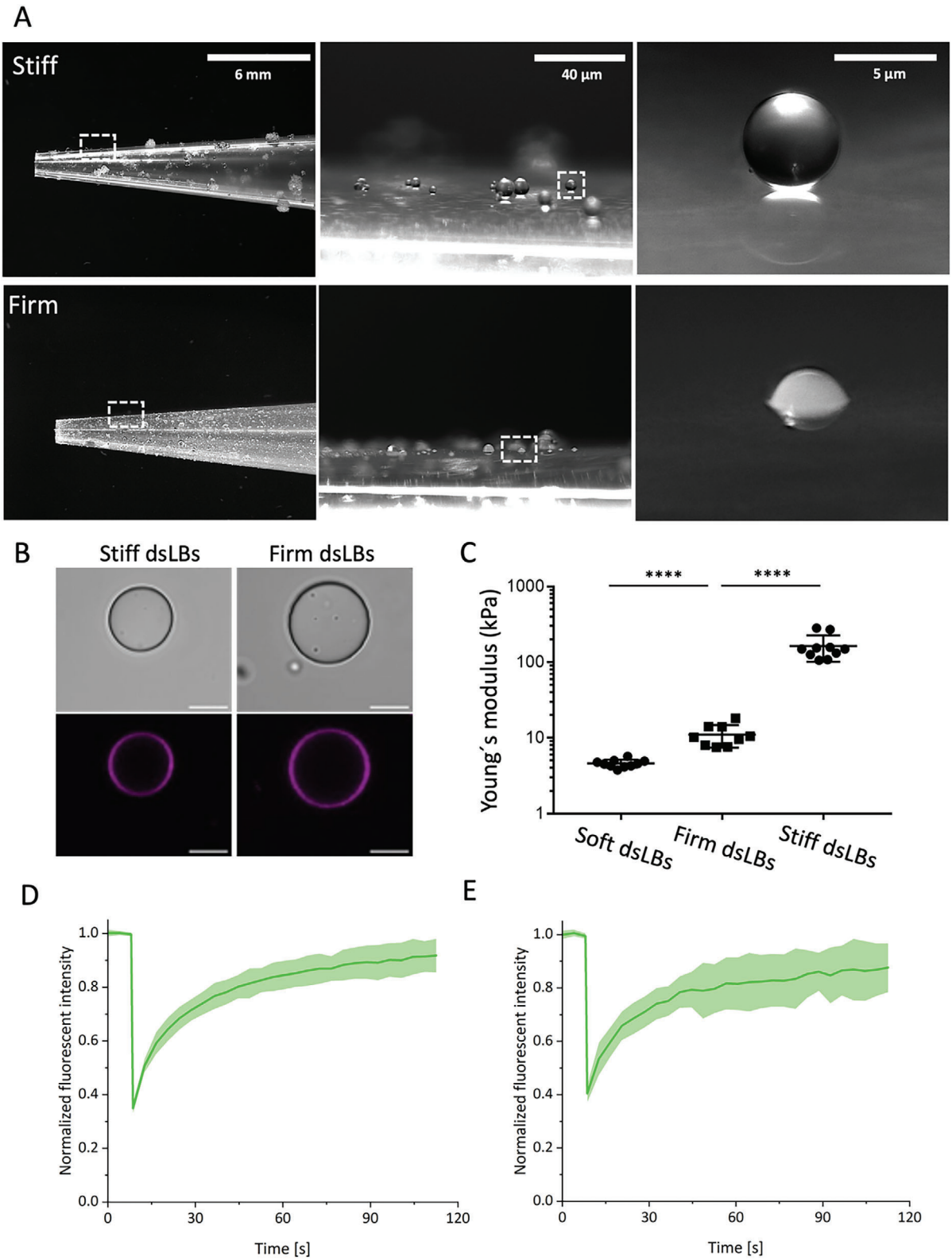

Figure 3. Tuning of dsLB stiffness. A) Stereomicroscopy images of stiff (top row) and firm (bottom row) dsLBs dried on plastic pipette tips at three magnifications. B) Representative confocal microscopy and bright field images of the lipid layer formed around stiff and firm dsLBs. Scale bars are 10 µm. C) Quantification of microscale Young´s moduli of soft, stiff and firm dsLBs by nano-indentation analysis. Results are shown as mean ±SD from n = 9 individual measurements. $^{****}p < 0.001$, unpaired two-tailed student t test. D and E) FRAP analysis of lipid layer mobility on stiff (D) and firm (E) dsLBs. Line indicates mean from n = 10 (D) and n = 9 (E) dsLBs, shaded green indicates standard deviation.

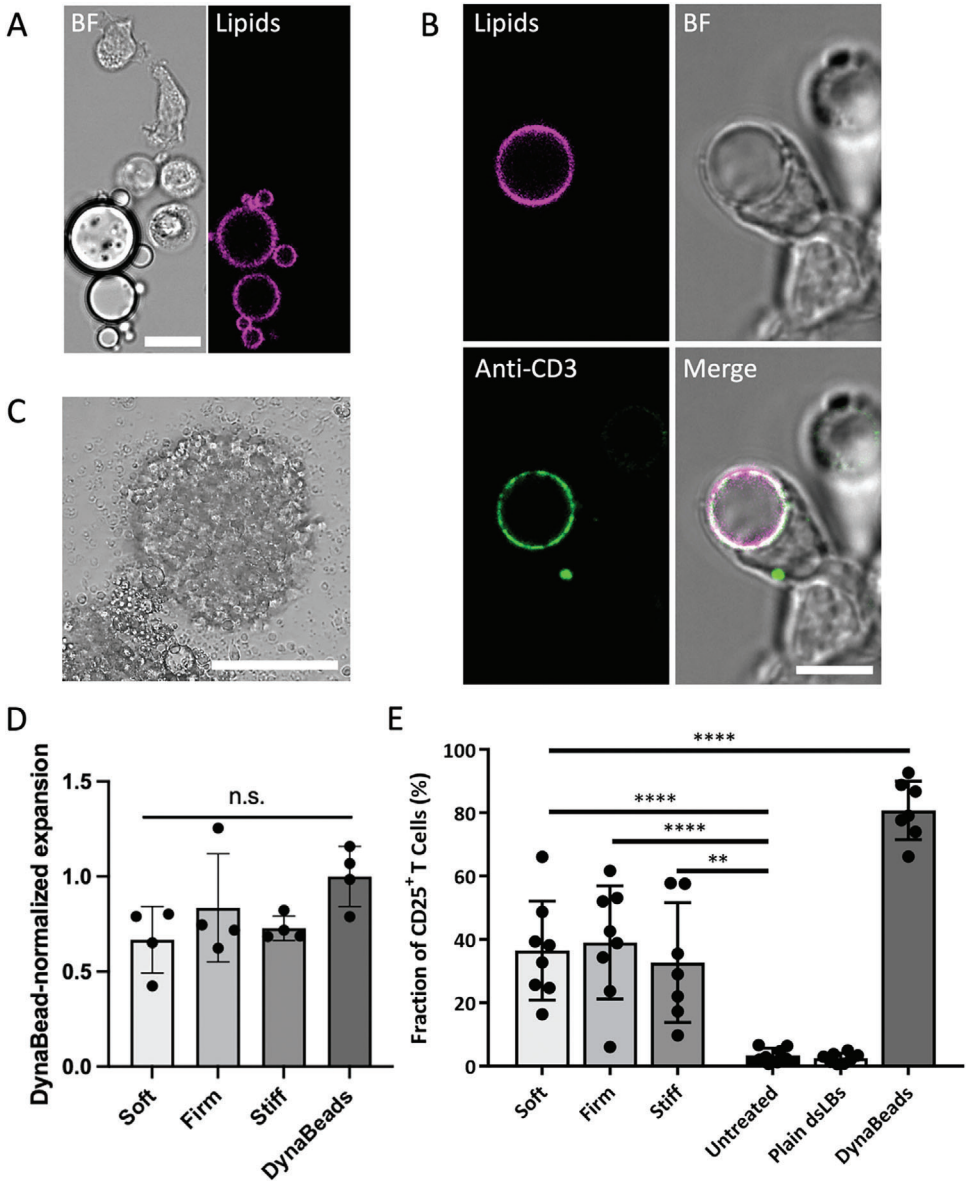

Figure 4. DsLB mediated T cell activation and expansion. A) Representative confocal microscopy and bright field images of co-cultivated T cell with dsLBs. Scale bar is 10 µm. B) Confocal imaging of a contact event between a T cell and a Rhodamine B labeled dsLB decorated with fluorescent anti-CD3 antibodies. Scale bar is 5 µm. C) Bright field microsopy image of an expanding T cell cluster induced by dsLB stimulation. Scale bar is 50 µm. D) Expansion fold quantification of T cells incubated with soft, firm and stiff dsLBs normalized to T cells expanded with DynaBeads. Results are shown as mean ±SD from n = two donors measured in duplicates. E) CD25 expressing T cell fractions of soft, firm and stiff dsLBs compared to untreated, plain dsLBs and DynaBeads control. Results are shown as mean ±SD from n = four donors measured in duplicates. $^{**}p < 0.01$ and $^{****}p < 0.001$, one way ANOVA test.

upregulated by ex vivo T cell expansion technologies.[36] Remarkably, we found significantly lower PD-1 expression as compared to DynaBead expanded cultures (**Figure** 5A). Again, no significant difference was observed between dsLBs of varying stiffness. Motivated by this PD-1^{low} T cell phenotype after dsLB expansion, we delved into a more detailed analysis to uncover their underlying functional properties. We conducted a multiplexed quantification of 12 key cytokines secreted by various T cell subsets (Figure 5B). Compared to DynaBeads, dsLB-expanded $CD8^+$ T cells secreted significantly lower levels of effector-associated cytokines, such as TNFα, FasL and granzymes. Intriguingly, dsLB-expanded $CD8^+$ T cells produced higher levels of regulatory and suppressive cytokines, specifically IL-4 and IL-10, compared to those expanded with DynaBeads. DsLB-expanded $CD8^+$ T cells also secreted significant amounts of the pro-inflammatory cytokine IL-17 and the regulatory cytokine INFγ, although to a lesser extent than DynaBead-expanded T cells. The secretion of these cytokines, typically associated with regulatory and helper T cells, was unexpected in $CD8^+$ cells and was not influenced by the stiffness of the dsLBs or their ligand density. This finding

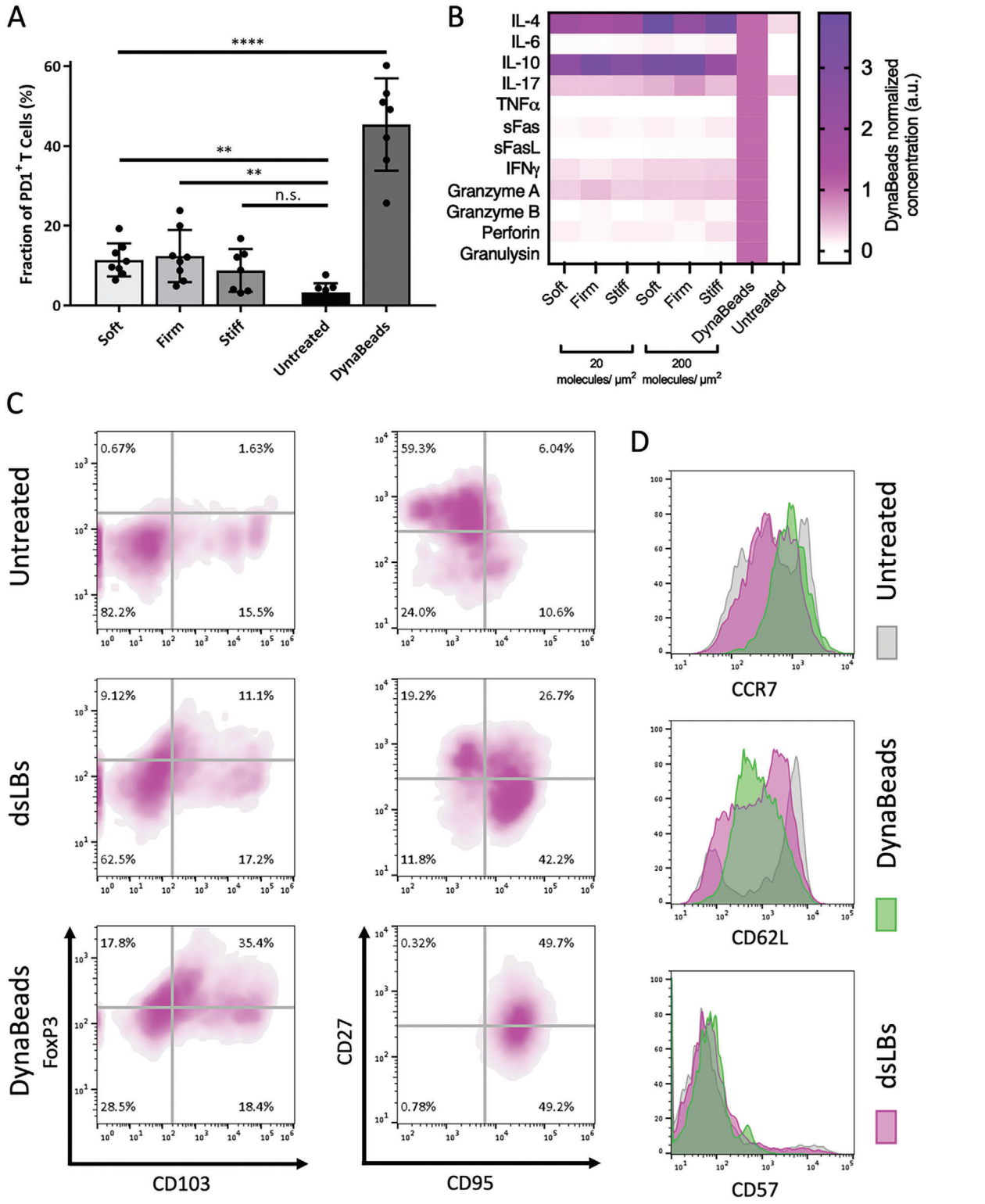

Figure 5. Phenotypic characterization of dsLB-expanded CD8$^+$ T cells. A) PD-1 expressing T cell fractions of soft, firm and stiff dsLBs compared to untreated and DynaBeads control. Results are shown as mean ±SD from n = four donors measured in duplicates. $^{**}p < 0.01$ and $^{****}p < 0.001$, one way ANOVA test. B) Concentration of released cytokines from T cells activated by soft, firm, stiff dsLBs with 20 or 200 antibodies/µm^2 on their membrane normalized each to the DynaBeads-treated culture and compared to an untreated controls. Results are shown as mean from n = two donors measured in duplicates. C and D) Flow cytometry analysis of CD8$^+$ T cells activated by soft dsLBs and stained for various surface markers. Untreated and DynaBeads activated T cells are shown as controls. Data is visualized as density plots for n>2000 single cells. Results are pooled from n = two donors measured in duplicates.

was also not attributed to CD4$^+$ T cell contamination from the CD8-specific negative selection process (Figure S11, Supporting Information). Although IL-4 and IL-10 producing CD8$^+$ T cells with a regulatory (Treg) or suppressive phenotype have been previously described,[37,38] their understanding remains limited, primarily due to inadequate expansion and isolation techniques as well as a lack of specific markers to identify them. To further characterize the dsLB-expanded T cell phenotype, we measured the expression of markers conventionally associated with CD8$^+$ Treg and memory differentiation (Figure 5C,D). Comparison of DynaBead- and soft dsLB-activated T cells revealed that both expansion approaches produced only minor increase in Foxp3$^+$ and CD103$^+$ expressing T cells, markers recently linked to CD8$^+$ Tregs.[39] However, expression of CD27, specifically in activated CD95$^+$ cells, as well as CCR7 and CD62L were differentially expressed in dsLB-expanded cultures as compared to DynaBeads. This indicates differentiation of a central to effector memory-like phenotype, with low level of senescent cells as measured by CD57 staining. Collectively, our data suggest that dsLBs preferentially expand a differentiated T cell subset with central- to effector-like memory marker expression, and IL-4/IL-10-based regulatory and suppressive properties, less susceptible to checkpoint inhibition (reduced PD-1 expression). All of which are favorable features for applications in adaptive cell therapy.

2.4. A 3D Parameters Space for T Cell Expansion

We noted that our results stand in some contrast to previous studies, which showed that variations in the stiffness of aAPCs significantly affected T cell activation. In our dsLB-based system, however, we did not observe such pronounced effects. This discrepancy may be attributed to our use of dispersed aAPCs with a laterally ligand mobility that facilitate molecular self-organization at the IS level. The lateral ligand mobility potentially masks or mitigates stiffness-related mechanosignaling in T cells, as previously also observed in other systems.[27] To explore this hypothesis, we assessed T cell expansion using non-deformable silica microbeads with orders of magnitude higher stiffness (70 GPa), coated with a lipid bilayer (memBeads) identical in composition to our dsLBs (**Figure 6A**), and functionalized with the same anti-CD3/CD28 antibodies through protein G coupling at the same density. These beads are comparable to DynaBeads in size (4.5 µm) and stiffness but additionally feature laterally mobile ligands. We found no significant difference in their ability to activate T cells, as determined by CD25$^+$ T cell quantification, compared to the order of magnitude softer dsLBs (Figure 6B). Interestingly, memBeads did also expand T cells with a PD-1^{low} expressing phenotype (Figure S12, Supporting Information). Of note, relevant parameters such as antibody clones, antibody densities, aAPC:T cell ratio and membrane composition were matched between the two aAPC substrates. This reinforces the notion that an aAPC membrane can mask aAPC stiffness-medited effects and is the major driver for the PD-1^{low} expressing phenotype.

Given the well-studied significance of mechanosignaling in T cell activation, which underlays the three most crucial biochemical signals (TCR activation, co-stimulatory ligands, cytokines), we investigated whether ligand mobility could also mask any effects based on variations on the level of biochemical signaling. Altering the anti-CD3 antibody (signal 1) from a UCHT1 clone to a lower-affinity SK7 clone, resulted in a decrease in CD25$^+$ cells, although eventual T cell expansion rates remained largely unaffected (Figure 6C,D). A similar outcome was observed when modifying the ratio of signal 1 and 2 stimulatory antibodies from 1:4 to 1:1, leading to a slightly smaller CD25$^+$ population with minimal impact on expansion rates. No significant stiffness-related differences were noted in any of these stimulation scenarios, including memBeads. Additionally, substituting the signal 2 stimulant, anti-CD28, with the integrin ligand ICAM1, resulted in a significant reduction of CD25$^+$ cells and minor variations in T cell expansion. Modifications on the level of signal 3, in our case IL-2, similarly affected T cell activation and expansion. When reducing the IL-2 levels from 50 to 12.5 U mL^{-1}, T cell expansion and CD25$^+$ cells was significantly decreased. Collectively, these findings suggest that while the lateral mobility of ligands on aAPCs can mask stiffness-related effects, the predominance of biochemical signaling over biophysical cues remains intact.

However, we figured that the biochemical signaling by agonistic CD3 antibodies was so potent that it might excel any subtile effects mediated by variations in stiffness. This could also be the case when the signaling intensity of the TCR trigger was reduced by using the SK7 anti-CD3 clone, a lower-affinity but still effective anti-CD3 agonist. Consequently, we hypothesized that using even lower biochemical signaling strength on signals I and II level might allow any latent stiffness-related effects, masked by the lipid membrane, to become more pronounced. This would suggest that biochemical signaling, substrate stiffness, and ligand mobility are three separate yet synergistic factors that contribute to the nuanced process of T cell activation. To further investigate this potential interplay, we designed a TCR stimulation configuration of lower signalling-strength that is also relevant to immunotherapy, by using a bispecific T cell engager (TCE) (Figure 6E). We formed dsLBs presenting the tumor-associated antigen (TAA) Her2, and adjusted the surface protein density to 100 (low) and 400 (high) molecules/µm^2 using MESF beads (Figure S13, Supporting Information). In conjunction with an ICAM1-based signal 2 and 50 U mL^{-1} IL-2 signal 3, a bispecific TCE targeting Her2 and CD3 was added to the dsLBs in CD8$^+$ T cell co-cultures to initiate signal 1. Here, dsLBs functioned as cancer target cell mimetics in a TCE-mediated in vitro-mimicked immunotherapy. The size of the Her2-TCE-CD3 complex is approximatly twice as large as the anti-CD3/TCR complex (see Supporting Note 1) and the kinetic seggragtion model[16] as well as previous data comparing IS formation efficacy between anti-CD3 agonists and bispecifc TCEs[40] suggest a lower stimulation strength of these dsLBs on T cells as compared to anti-CD3/CD28 dsLBs. Confocal microscopy demonstrated successful adhesive contact formation between Her2-dsLBs and T cells. Moreover, we observed re-localization of AlexaFluor488-labelled Her2 at the cell interface, indicating successful TCE coupling and IS formation (Figure 6F). We then quantified the IC50 of the TCE and its maximum activation potential (as indicated by CD25 upregulation) for two ligand densities on soft and firm dsLBs (Figure 6G). Stiff dsLBs were not included in the analysis as their stiffness exceeded the stiffness range of cancer cells by several orders of magnitude and is therefore most likely not relevant for TCE therapies.[41,42] Markedly, the IC50 values

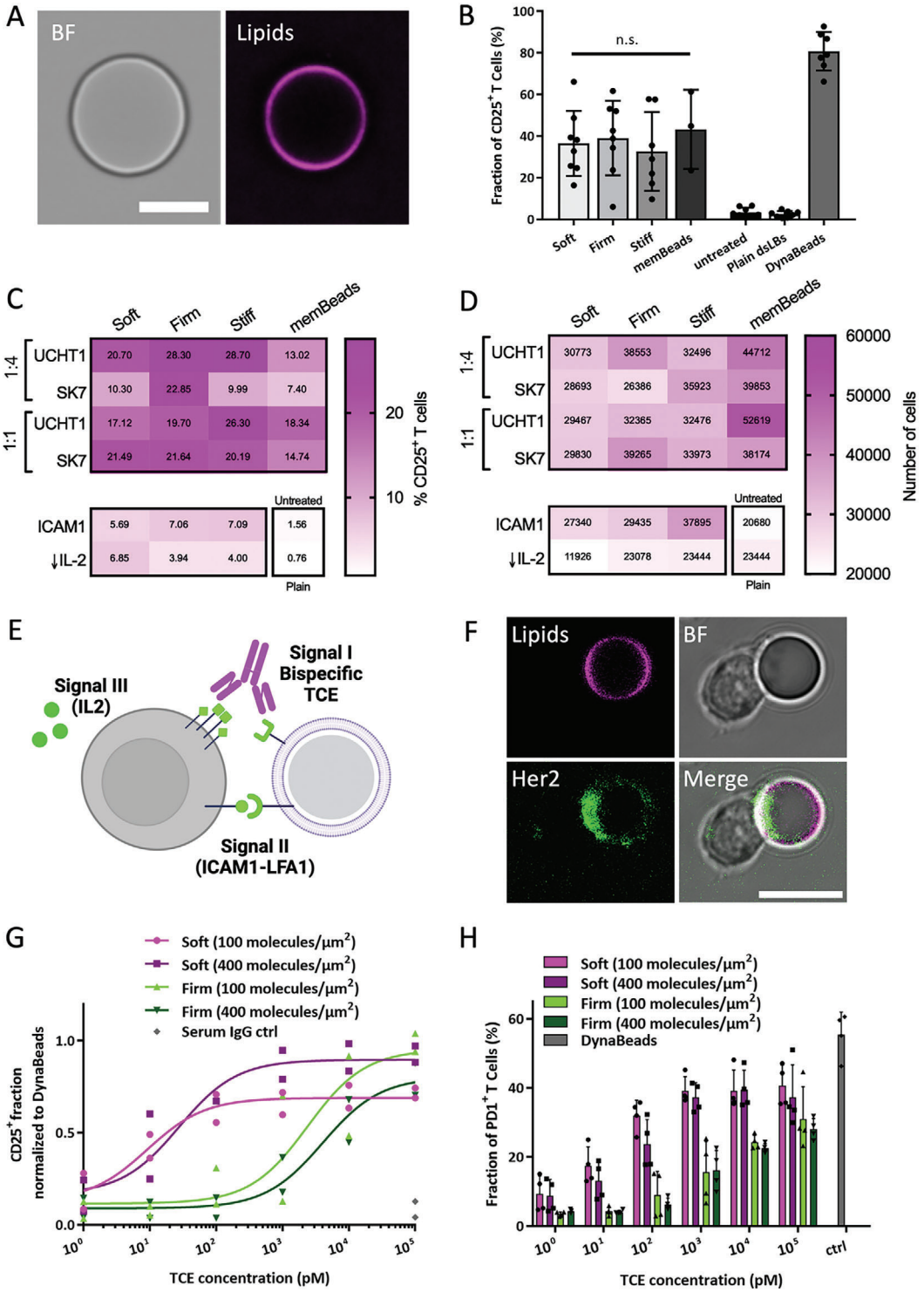

Figure 6. Role of biochemical and biophysical cues for T cell expansion. A) Representative bright field and confocal microscopy images of silica beads coated with a fluorescence lipid membrane. Scale bar is 2.5 μm. B) Flow cytometry quantification of $CD25^+$ $CD8^+$ T cells after expansion with different aAPC technologies. Results are shown as mean ±SD from n = four donors measured in duplicates. C and D) Flow cytometry quantification of $CD25^+$ $CD8^+$ T cells (C) and expansion quantification (D) of $CD8^+$ T cells, after stimulation with aAPC presenting various configuration for signals I,II and III. Results are shown as mean from n = four donors measured in duplicates. E) Schematic representation of the bispecific TCE stimulation setup with dsLBs. F) Representative confocal microscopy images of a primary $CD8^+$ T cell incubated with bispecific TCE and dsLBs (membrane in magenta) presenting the TAA Her2 (green). Scale bar is 10 μm. G and H) Flow cytometry-based quantification of $CD25^+$ (G) T cell populations normalized to DynaBead-expanded and $PD\text{-}1^+$ (H) T cell populations in a TCE dilutions series incubated with Her2 presenting dsLBs of varying stiffness. Results are shown as mean ±SD from n = two donors measured in duplicates.

differed significantly by two orders of magnitude between the soft and firm dsLBs. Also the maximum activation efficiency was impacted by substrate stiffness and Her2 density. These results confirmed that substrate stiffness can influence T cell activation even when ligands are laterally mobile but particularly when biochemical signaling strength is lowered, which suggest a trigger hierarchy for T cell activation where biochemical signals provide the most potent cue, followed by biophysical cues related to lateral ligand mobility and finally the stiffness of the aAPC itself (biochemical signaling > ligand mobility > substrate stiffness).

Crucially, we also evaluated PD-1 expression in this TCE setup and observed that the PD-1 expressing population remained significantly lower across both dsLB stiffnesses as compared to DynaBead positive controls (Figure 6H). This outcome indicates that it is foremost the introduction of laterally mobile ligands that fosters a T cell phenotype with a reduced susceptibility for immune suppression.

3. Summary and Outlook

In this study, we introduced a new aAPC technology that is inspired by bottom-up synthetic biology principles and designed to mimic the biophysical properties of APC membranes. The dsLB technology combines lateral membrane mobility and stiffness modulation to integrate an additional biophysical cue that can tune the interactions between T cells and aAPCs. Previous studies has focused on the mechanobiological component of T cell activation,[8] but the importance of lateral ligand mobility in this context has not been extensively studied due to a lack of suitable methods that integrate both aspects. While solid-bead and planar supported lipid bilayers have been used to study the formation dynamics of IS,[43] it has been challenging to dissect the individual contributions and functional implications of stiffness and mobility cues for the expansion of therapeutic T cells with suitable dispersed expansion systems. Our findings confirm that mechanical cues together with lateral ligand mobility provide a biophysical context for receptor-ligand-mediated T cell activation. They also demonstrate how T cell differentiation can be guided by such biophyical cues and highlight that lateral ligand mobility is an important feature for the design of effective aAPC technologies. Moreover, our observation that dsLBs produced a smaller population of PD-1-expressing T cells after expansion suggests that membrane mobility could be central to direct the differentiation process during ex vivo T cell expansion for therapeutic approaches. As this was also observed in silica bead-supported membranes and in our bispecific T cell engager system, the lateral ligand mobility and not stiffness-related cues might be central to this effect.

Most importantly, we found that dsLB expand a $CD8^+$ T cell phenotype that secrets the anti-inflammatory and regulatory cytokines IL-4 and IL-10. These are conventionally associated to $CD4^+$ T regulatory cells but have been described for $CD8^+$ T cells on multiple occasions, including their potential role for immunotherapy.[44] Immunotherapeutic approaches based on $CD8^+$ regulatory T cells are currently impeded by a lack of suitble ex vivo expansion technologies that preferentially expand this phenotype over effector cytolytic $CD8^+$ T cells. Although extensive functional analysis of dsLB-expanded T cells remains do be performed to assess their suppressive and cytolytic potential in a therapeutic context, their surface marker expression profile suggest a differentiation stage close-associated to effector- and central-memory T cells.

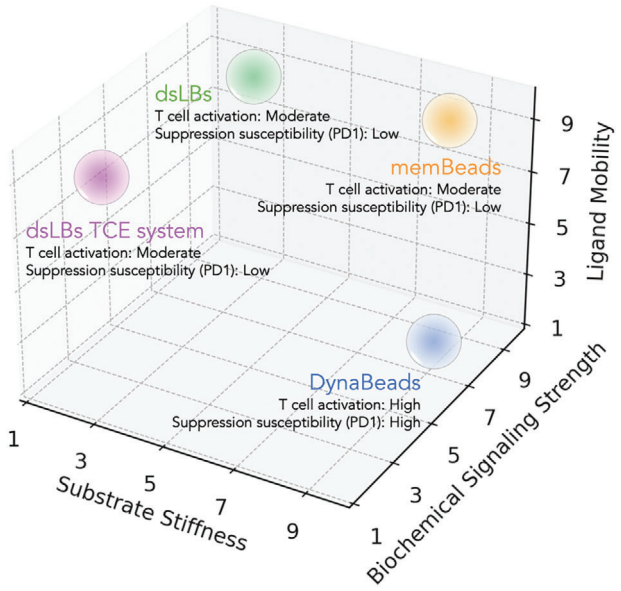

Figure 7. A 3D space for aAPC-based T cell expansion. Schematic plot for the four aAPC technologies tested in this study over biochemical signaling, substrate stiffness and lateral ligand mobility indicating that illustrating the synergistic contribution of these three cues for T cell expansion and the importance of lateral ligand mobility for a PD-1-expressing phenotype.

We benchmarked the dsLB technology to a widely applied solid bead-based approach (DynaBeads). These are a globally established technology. Although expansions rates achieved with dsLB were consistantly lower, the smaller percentage of PD-1-expressing T cells and their pronounced differences in IL-4 and IL-10 secretion, position dsLBs as a potential addition to this approach, expanding the repertoir for therapeutic T cell expansion.

Of note, the observed effects on T cell activation and differentiation were not mediated by stiffness-related biophysical cues but most likely by the presentation of stimulatory ligands on laterally mobile membrane. In this context, the pivotal role of receptor organization at the IS for T cell activation is general consensus in the field.[17] DsLBs provide a first aAPC technology for of generation dispersed, low-stiffness and scalable particles with laterally mobiles ligands. As stiffness-related effects were not as prevalent as observed in other studies, our systematic analysis of the impact of substrate stiffness and the signaling strength of signal I, II and III on T cell activation suggest a 3D physico-chemical space of T cell activation (**Figure 7**). In this space, lateral ligand mobility appears to be the major switch for PD-1 expression. Potentially, the lipid bilayer on the dsLB surface facilitates lateral ligand mobility, effectively masking the effects of substrate stiffness by limiting the T cells' ability to exert significant traction forces necessary for probing mechanical cues.

DsLBs have further interesting applications in biomaterial-science and synthetic biology. While previous studies have described the formation of PDMS droplets for sensing purposes, only a few have demonstrated their potential for use in biomedicine.[7,45–47] In our study, we achieved adjustable

stiffness of these PDMS droplets by using a differential curing process. We also developed a new approach for functionalizing and stabilizing the dispersed droplets in solution using ionic surfactants to create a charge-mediated lipid bilayer on the droplets. This approach, together with the magnetic NP-based separation, has significant implications for up-scaling the technology and increasing its applicability. Moreover, as our electron microscopy observations and shelf-life experiments suggest, it confers stability to the emulsions to avoid droplet aggregation or unmixing. Therefore, by providing a new avenue for crafting lipid bilayers onto droplets, we have expanded the potential uses of dsLBs in biomedicine and beyond. Potential improvements for the technology include implementation of a membrane extrusion-based or microfluidic-assisted emulsification process to increase monodispersity of the dsLBs.[25] Furthermore, additional co-regulatory ligands, such as CD58 or membrane-immobilized IL-2, could be integrated into a dsLB system to provide additional means for directing the differentiation process.[48] DsLBs could find application in areas such as drug delivery, biosensors, and tissue engineering, where it could provide a more versatile and effective alternative to existing biomimetic synthetic cell techniques. In summary, by harnessing the power of bottom-up synthesis of synthetic cells as cellular bionics of aAPCs, we devloped a new approach for T cell activation able to mimic central biochemical and biophysical characteristics of APC.

4. Experimental Section

DsLB Assembly: DsLBs were assembled following the strategy illustrated in Figure 1. For this, ≈100 mg of PDMS (Sylgard 184, Dow Corning USA) were mixed with 880 µL PBS containing SDS (1 mM if not specified otherwise) and manually pre-emulsified by resuspension. The solution was then transferred to a sonication bath for 2 min at room temperature to produce a dispersed o/w emulsion. Subsequently, $MgCl_2$ (Sigma–Aldrich, Germany) was added to a final concentration of 20 mM (if not specified otherwise) together with 100 µL of 6 mM (final lipid concentration) SUV solution to form dsLBs. SUVs, consisting of 20 mol% EggPG, 5 mol% PE-DGS-NTA(Ni^{2+}), 1 mol% LissRhodamine B-PE or Atto488-PE and 74 mol% EggPC (all Avanti Polar Lipids, USA) were produced by extrusions as described previously.[25] The dsLB solution was incubated at room temperature protected from light for 2 min and subsequently centrifuged at 8600 × g for 30 s. The supernatant was discarded and the dsLB pellet was resuspended in 1 mL PBS for one additional centrifugation step with the parameters specified above. The dsLB solution was resuspended in 1 mL PBS and stored at 4 °C and protected from light until further usage. For control experiment, 1 mM Triton X-100 (ACROS Organics) was used instead of SDS. Where indicated, dsLBs were also formed from other silicon oils, specifically AR20 (Sigma–Aldrich, Germany), AP100 (Sigma–Aldrich, Germany) as well as highly thermostable silicon oil (SO) (Merck, Germany).

For protein functionalization, the total amount of accessible dsLB membrane present in a dsLB preparation lot was measured by calibrating against a SUV dilution series with known concentration. For this, a SUV dilution (same lot as used for dsLB production) was prepared in a 96 well plate. The fluorescence intensity (originating from the Rhodamine B) in each dilution was measured with a TECAN Spark (Tecan Group, Switzerland) plate reader controlled by TECAN SparkControl software with in-built gain optimization and excitation/emission setting adjusted to 537/582 nm, to derive a fluorescence-concentration calibration curve. The total lipid concentration of a dsLB solution was obtained by measuring the fluorescence intensity alongside the SUV dilution series and referencing to the calibration curve. From the final lipid concentration, the concentration of total accessible DGS-NTA(Ni^{2+}) was derived. Protein G (Sigma Aldrich, Germany) was added at the molar ratio specified in the figure legends and incubated for binding to the NTA(Ni^{2+}) moieties at 4 °C protected from light for 60 min. The dsLBs were subsequently washed by centrifugation before adding IgG antibodies against human CD3 (UCHT1, Invitrogen), CD28 (CD28.2, Invitrogen), CD8 (SK1, BioLegend) or CD3-AlexaFluor488 (HIT3a, BioLegend) in a 1:2 protein G to IgG ratio. Moreover, the ratio of CD3 and CD28 antibodies was adjusted to be 1:4. The IgGs were incubated for at 4 °C protected from light for 30 min to bind to the protein G on the dsLBs and residual IgG were then washed off by centrifugation and the final dsLB lipid concentration was quantified by plate reader quantification as detailed above.

Cross-Linking of dsLB Oil Cores: Aiming for an adjustable stiffness of dsLBs, the PDMS oil core was crosslinked. For this, the PDMS oil was thoroughly mixed in a 10:1 (stiff dsLBs) and 50:1 (firm dsLBs) ratio with Silicon Elastomer Curing Agent (Sylgard 184, Dow Corning USA) and then resuspended in 880 µL PBS containing 1 mM SDS. This oil in water emulsion was sonicated for 2 min and subsequently cured over night at 60 °C in a water bath. From the cured droplets, dsLBs were produced as described above.

Environmental Scanning Electron Microscopy: For ESEM-based analysis, dsLBs from a standard lot (1 mM SDS, 20 mM $MgCl_2$) were pelleted by centrifugation and resuspended in 100 µL PBS. A 5 µl droplet of this solution was placed on an FEI Quanta 400 FEG equipped with an ESEM Peltier stage operating at 3 °C and transferred to the microscope chamber. A water vapor pressure of 750 Pa was selected to start at fully wet conditions. Then the water vapor pressure was stepwise decreased resulting in a shrinkage of the water droplet due to evaporation of water. Individual dsLBs were visualized at different water vapor pressures at 3 °C.

CryoTEM: For cryoTEM a 2 µL droplet of the sample solution was placed on a holey carbon film (Plano, S147-4), blotted for 2 s and vitrified in liquid ethane using a Gatan CP3 plunge-freezer operating at −165 °C. The resulting cryoTEM sample was transferred to a Gatan model 914 cryoTEM sample holder and imaged by bright field transmission electron microscopy (JEOL JEM 2100 LaB6) at 200 kV accelerating voltage under low-dose conditions. For image acquisition a Gatan Orius SC1000 CCD camera was used (exposure time 2 s).

TEM-EDX: For TEM-EDX a droplet of the sample solution was placed on a holey carbon covered copper grid (Plano, S147-4) and dried under ambient conditions. Bright field transmission electron microscopy (JEOL JEM 2100 LaB6 equipped with a Gatan Orius SC100 CCD camera) at 200 kV accelerating voltage was done in combination with X-ray spectral analysis (EDX, Thermo Noran NSS7) to determine the chemical composition of the sample after drying. The acquisition time for EDX was <10 s.

Dynamic Light Scattering: Zeta potentials of dsLBs and SUVs were measured with a Malvern Zetasizer Nano ZS system. Equilibration time was set to 30 s at 25 °C, followed by three repeat measurements for each sample at a scattering angle of 173° using the built-in automatic run-number selection. The material refractive index was set to 1.460 and the absorption to 0.010 and solvent properties to $\eta = 0.8882$, n = 1.33 and $\epsilon = 79.0$. All measurements were performed in 1X phosphate buffered saline (pH 7.4).

NBD Assay: For assessment of lipid layer configuration by NBD assays, a modified protocol, published previously, was applied. DsLBs were formed from 20 mol% EggPG, 1 mol% PE-DGS-NTA(Ni^{2+}), 1 mol% 16:0-12:0 NBD PE and 78 mol% EggPC (all Avanti Polar Lipids, USA) SUVs. NBD fluorescence was measured with a Tecan Spark plate reader controlled by TECAN SparkControl software with an in-built gain optimization and excitation/emission setting adjusted to 468/537 nm. A dithionite (Sigma–Aldrich, Germany) dilution series between 0.2 and 50 mM was prepared in a 96 well plate and dsLBs were added to a final concentration of 60 µM total lipids (assuming that all SUVs were incorporated in the dsLB membrane). The fluorescent intensity and the amount of NDB fluorophores were correlated using a SUV dilution series and the non-linear fluorescent intensity of dsLBs was corrected with a serial dilution of dsLBs. Both calibrations were prepared and measured within the same well plate to derive a fluorescent intensity to NDB fluorophores calibration curve. The number of fluorophores was normalized to the dithionite untreated

control. As dithionate was a strong acid, all experimental steps were performed in PBS + 100 mM HEPES.

Confocal Microscopy: Confocal microscopy was performed using a laser scanning microscope LSM 880 (Carl Zeiss AG). Images were acquired using a 20x (Plan-Apochromat 20x/0.8 M27, Carl Zeiss AG, Germany) and a 63x immersion oil objective (Plan-Apochromat 63x/1.4 oil DIC M27, Carl Zeiss AG, Germany) and 488 and 543 nm laser lines. Images were analyzed using ImageJ (NIH, USA) software. For imaging, dsLBs were dissolved 1:20 or 1:40 in 8-well Nunc LabTeK glass bottom chamber slides filled with 200 µL PBS.

Size Distribution Analysis: For dsLB size distribution analysis, dsLBs were imaged by confocal microscopy with a LSM 880 (Carl Zeiss AG) equipped with a 20x objective and excitation/emission setting adjusted to 458/543 nm. Z-stacks over the fully dsLB height were acquired from which maximal z projections were produced. Particle sizes were measured with ImageJ software (NIH, USA) by global intensity-threshold segmentation, watershed particle separation and automated particle detection.

Fluorescence Recovery after Photobleaching Analysis: FRAP experiments were performed with a laser-scanning microscope LSM 880 (Carl Zeiss AG) equipped with a 63x objective. The Rhodamine B in the membrane was replaced by Atto 488-PE. Bleaching areas in the equatorial plane of the dsLBs with a minimum of radius of 5 µm were selected and bleached with a 100% 488 nm laser intensity. A minimum of 3 pre-bleaching and 27 post-bleaching images were acquired. Mean fluorescence intensity time profiles for the bleached area, the whole dsLB and background fluorescence were measured with ImageJ (NIH, USA) software. Profile background and intensity normalization as well as data fitting, calculation of mobile fractions and calculation of $t_{1/2}$ maximum was performed with easyFRAP web-based tool (Zoi Lygerou, University of Patras).

MESF Bead Assay: DsLBs were assembled and the concentration of DGS-NTA(Ni^{2+}) calculated as described above. To account for potential unspecific binding of Protein G or antibodies, additional dsLBs without DGS-NTA(Ni^{2+}) were produced. To functionalize the dsLBs, samples were mixed with different quantities of protein G. The following molar ratios of protein G to DGS-NTA(Ni^{2+}) were used; 1:8, 1:4, 1:2, 1:1 and 2:1. For the DGS-NTA(Ni^{2+})-free dsLBs, the same amount of Protein G was used as in the 1:2 mixtures. All samples were incubated at 4 °C for 45 min and subsequently washed by centrifugation. Alexa Fluor 488-labelled anti-CD8 (SK1, BioLegend, UK) were added to every sample, with the antibody concentration being adjusted to 150% of the respective initial protein G concentration. The samples were protected from light, incubated at 4 °C for 45 min and washed again by centrifugation. A cocktail of Quantum Alexa Fluor 488 MESF beads (Bangs Laboratories Inc., USA) was prepared according to the suppliers' instructions. DsLBs were premixed 1:1 with the bead cocktail and dissolved 1:10 in 8-well Nunc LabTeK glass bottom chamber slides filled with 200 µL PBS. Imaging was performed with a LSM 880 (Carl Zeiss AG) using a 20x objective and 488 nm excitation. The ImageJ (NIH, USA) software was used for watershed particle separation, automated particle detection and measurement of the mean fluorescent intensity of individual particles. The beads were identified by their lack of Rhodamine B fluorescent signals and uniform size and used to generate a calibration curve to correlate fluorescent signal to MESF. The mean number of antibodies on the dsLBs was calculated and used to generate another calibration curve linking the amounts of protein G/antibody used to the number of antibodies bound to the particles surface.

Real Time Deformation Cytometry: The Young's modulus of non-cured dsLBs was measured using an AcCellerator (ZellMechanik Dresden, Germany), a commercial real-time deformation cytometer (RT-DC). The RT-DC analysis was based on the introduction of flow into a microfluidic chip using syringe pumps, where dsLBs were deformed by hydrodynamic stresses as they passed through a narrow constriction that was larger than their size. Imaging was performed using an inverted microscope (Axiovert 200 M, ZEISS, Germany), and images were acquired at the end of the microfluidic constriction using a CMOS camera (Mikrotron, Germany). The ShapeIn software (Zellmechanik Dresden, Germany) was used to control both the camera and syringe pump. To analyze the recorded images in real-time, enabling computation of a contour and projected area for each dsLB the ShapeOut 2 software (Zellmechanik Dresden, Germany) was used. To exclude dsLB doublets or debris, area limits were set to 80 and 250 μm^2 and deformation limits were set to 0.003 and 0.008. For measurements of dsLBs, samples were diluted according to a Mcfarland standard of 6 MFS with a viscosity-adjusted measurement CellCarrier buffer (Zellmechanik Dresden, Germany), which increased the stresses acting on the dsLBs inside the channel. Measurements were performed using microfluidic channels with a width of 20 µm at a flow rate of 0.025 µL s^{-1}.

Iron Oxide Nanoparticles Synthesis: Iron oxide nanoparticles (NPs) were synthesized as described in.[49] Specifically, 6 mmol Iron(III) acetylacetonate (Sigma–Aldrich, 97%) were dissolved in 30 mL dibenzyl ether (Sigma Aldrich, ≥ 98.0% GC) and 30 mL oleylamine (Acros Organics, 80% – 90%). The solution was heated to 110 to 130 °C for 1 h under continuous nitrogen flow. Afterwards the solution was heated to 300 °C at a heating rate between 15 and 20 °C min^{-1} under constant nitrogen atmosphere and maintained at 300 °C for 1 h. The dispersed NPs were cooled down to room temperature and washed 3 times with a mixture of isopropanol and acetone (50/50). Finally, the NPs were dispersed in toluene at a concentration of 40 mg mL^{-1}. Ligand exchange to Poly(dimethylsiloxane), ω-(carboxy decyl)-terminated (Polymer Source, P18578-DMS-C_{10}COOH) was performed as following: 20 mL of the 40 mg mL^{-1} iron NP dispersion was heated to 80 °C under stirring. After reaching the temperature, 1 mL of the ligand was added to the dispersion. The mixture was stirred at 80 °C for 24 h. Afterwards the dispersion was cooled down and washed 3 times with ethanol and finally dispersion in 20 mL of hexane (Sigma–Aldrich ≥ 95%).

Compression Rheology: To measure the elastic modulus of PDMS bulk material for stiff and firm dsLBs, PDMS was cross-linked 10:1 and 50:1 with Curing Agent in a 24-well plate at 60 °C over night in a drying cabinet. The cured PDMS bulk was stamped to a diameter of 10 mm, resulting in PDMS blocks with a 1:1 diameter to high ratio. The elastic moduli of the stamped PDMS bulk cylinders were measured by compression rheology using Z100 (ZwickRoell, Germany) equipped with a 200 N load cell and a 40 mm compression die. The test speed for the PDMS bulk compression was 1 mm min^{-1} while the pre-load was 0.10 N for stiff and 0.05 N for firm PDMS bulk material.

Nano-Indentation Analysis: To confirm the elastic moduli for PDMS bulk material the samples were measured using the Pavone nano-indenter (OPTICS11 life, Netherlands). For this purpose, the bottom of 48 well plates were coated with non-cured, degased PDMS cross-linked 10:1 with Curing Agent. DsLBs were prepared according to the protocol in cross-linking of dsLB oil cores, in order to stabilize the dsLBs. 50 µL of the dsLB suspension was mixed with 950 µL of PBS and added to the coated wells. The samples were cured at 60 °C over night in a drying cabinet. BSA was added to the PBS to a final concentration of 1% and incubated at RT for 10 min. The dsLBs were probed with an indentation of 800 nm using a cantilever with a tip diameter of 3 µm and a stiffness of 0.53 N m^{-1}. The data was processed and analyzed using the inbuild software and a Herzian Fit.

T Cell Isolation and Culture: Human primary $CD8^+$ T cells were routinely cultured in RPMI 1640 w/ L-Glutamine (VWR, Germany) medium supplemented with 10% fetal bovine serum (Gibco, Germany), 1% penicillin/streptomycin (Gibco, Germany), 1% non-essential amino acids (Biowest) and 50 mM HEPES (Sigma–Aldrich, Germany) in cell culture treated flasks at 37 °C, 5% CO_2 and 100% humidity. For $CD8^+$ culture and expansion as well as for all functional assays, 50 U mL^{-1} recombinant human IL-2 (STEMCELL technologies, Germany) were added to the culture medium. Primary human $CD8^+$ were isolated from leukapheresis reduction system (LRS) chambers from de-identified, voluntary healthy blood donors with commercially available negative selection kits (RosetteSep Human $CD8^+$ T cell Enrichment Cocktail, STEMCELL technologies, Germany) following the manufacturers instruction. Blood samples were provided by the Institute for Clinical Hemostaseology and Transfusion Medicine, Saarland University Medical Center, following ethics agreement number 34/23 (Ethikkommission Ärztekammer des Saarlandes). The cells were either used within 2 days for experiment or cryopreserved.

T Cell Activation and Expansion with dsLBs and Flow Cytometry Analysis: Activation and expansion of primary human $CD8^+$ T cells was performed in 96 well plate formats by incubation of 70 000 T cells in an ≈1:2 ratio with

dsLBs in a total volume of 250 µL. For all tested conditions a final concentration of 50 U mL^{-1} recombinant human IL-2 was added. Expansion was performed for 7–9 days at 37 °C, 5% CO_2 and 100% humidity in fully supplemented cell culture medium. dsLBs were conjugated with the indicated antibody densities immediately before the experiment. For control experiments, a final concentration of soluble anti-CD3 (UCHT1, Invitrogen) and anti-CD28 (CD28.2, BioLegend, UK) antibodies of 187.5 ng mL^{-1}, or plain dsLBs without conjugated antibodies were added to the cells. As positive controls, Dynabeads human T-Activator CD3/CD28 beads (Gibco, Germany) were used following the manufacturers recommendations. After the expansion period, the cell solution was resuspended and transferred to a round bottom 96 well plate. Cells were pelleted at 300 x g for 5 min, the supernatant was disposed and the cell pellet was resuspended in PBS + 1% BSA containing the staining antibodies (1:400) and incubated for 30 min at RT protected from light. For the surface marker staining AlexaFluor488 or AlexaFluor647, FITC or PerCP/Cyanine 5.5 conjugated staining antibodies against CD25 (BC96, BioLegend, UK), PD-1 (NAT105, BioLegend, UK), CD8 (SK1, BioLegend, UK), CD4 (OKT4, BioLegend, UK), FOXP3 (259D, BioLegend, UK), CCR7 (G043H7, BioLegend, UK), CD62L (DREG-56, BioLegend, UK), CD103 (Ber-ACT8, BioLegend, UK), CD57 (HNK-1, BioLegend, UK), CD95 (DX2, BioLegend, UK) or CD122 (TU27, BioLegend, UK) were used. Cells were then washed by centrifugation and resuspension in PBS containing 1% BSA to remove unbound antibodies. After an additional centrifugation step, cells were fixed in 2% PFA (Sigma–Aldrich, Germany) for 30 min at room temperature and protected from light. The PFA solution was removed by centrifugation and cells were stored until further analysis in PBS containing 1% BSA at 4 °C protected from light. Surface marker staining was quantified with a Luminex Guava easyCyte and FACSVerse flow cytometer (BD Biosciences) equipped with 642 and 488 nm laser lines. A minimum of 1000 cells was recorded for each condition. The flow cytometric data was analyzed via the FlowJo V.10 software (FlowJo LLC, USA).

Cytokine Analysis using Flow Cytometry: In order to gain a better understanding of dsLB expanded T-cell phenotyps, a LEGENDplex Human CD8/NK Panel V02 (BioLegend, UK) was performed. For this, primary human $CD8^+$ T cells were co-cultured with soft, firm and stiff dsLBs, DynaBeads as well as memBeads. These aAPCs were decorated with anti-CD3 (UCHT1 or SK7, Invitrogen) as primary stimulating signal and anti-CD28 (CD28.2, BioLegend) co-stimulatory signal in ratios of 1:4 or 1:1 with a final AB concentration of at 200 molecules μm^2. To take co-stimulatory signals for T-cell expansion into account CD28 was replaced by ICAM1 (Sino Biological, China) or IL-2 was reduced to 12.5 U mL^{-1}. The co-cultivations was performed with 70 000 $CD8^+$ T-cells in a 1:2 ratio with aAPC in 96-well plates for 7–9 days at 37 °C, 5% CO_2 and 100% humidity in fully supplemented cell culture medium. After the incubation the cells were centrifuged and 100 µL of the supernatent was used to conduct the LEGENDplex assay. It was performed according to manufacturer instructions and measured using FACSVerse flow cytometer. Cytokine concentrations were assessed by analysing the data with a software suitable for LEGENDplex provided by BioLegend (https://www.biolegend.com/en-us/immunoassays/legendplex/support/software).

$CD8^+$ T-Cell Expansion Analysis: T cells from the previously described LEGENDplex assay were fixed with 2% PFA for 30 min at RT in the 96-well plate. After the fixation 2% BSA were added for 10 min before the cells were incubated for 1 h with the nucleus staining fluorophor Hoechst 33342 (Thermo Fisher scientific, Germany) at a final concentration of 1 µg mL^{-1}. The stained cell nulcei were imaged with a LEICA DMI600 B (Leica Microsystems, Germany) and a 10x objective (HCX PL FLUOT AR 10x/0.30, Leica Microsystems, Germany) and UV excitation. The images were analyzed with the ImageJ software (NIH, USA) by global intensity-threshold segmentation, watershed particle separation and automated cell counting.

T Cell Stimulation with dsLBs and a Bispecific T Cell Engager: $CD8^+$ T cells were activated and expanded in 96 half-area well plates by incubating 50 000 T cells in a approximate ratio of 1:2 with dsLBs in a total volume of 180 µL fully supplemented cell culture medium for 9 days. All conditions were further supplemented with recombinant human IL-2 at a concentration of 50 U mL^{-1}. The incubation conditions were 37 °C, 5% CO_2 and 100% humidity. The dsLBs were decorated with Her2 (Sino Biological, China) and ICAM1 (Sino Biological, China) using the same method as previously described for protein G functionalization, with the final Her2 protein density being 100 and 400 molecules μm^2. A CD3/Her2 bispecific T cell engager (BSAB-002, Creative Biolabs, USA) was added to the medium in a 6 step dilution series reaching from 1 pM to 100 000 pM. After 4 to 5 days of incubation, the antibody containing medium was exchanged for fresh cell culture medium without additional TCE. Four control experiments were performed: T cells were incubated without dsLBs or with non-functionalized, plain dsLBs. T cells were co-cultured with dsLBs decorated with 100 Her2 molecules μm^2, while the cell culture medium was supplemented with a final concentration of 100 000 pM of human serum IgG (I4506, Sigma–Aldrich, Germany). Lastly, Dynabeads human T-Activator CD3/CD28 beads (Gibco, Germany) served as a positive control and were used according to the manufacturers recommendations. The T cells were stained with AlexaFluor488 or AlexaFluor647 conjugated antibodies against CD25 (BC96, BioLegend, UK) and PD-1 (NAT105, BioLegend, UK) and fixed in in 2% PFA (Sigma–Aldrich, Germany) as described above. The surface marker staining was documented using Luminex Guava easyCyte and FACSVerse flow cytometers. A minimum of 2000 cells were recorded for each condition. The flow cytometric data was analyzed via the FlowJo V.10 software (FlowJo LLC, USA).

Data Post-Processing and Statistical Analysis: Graphs were plotted either with GraphPad Prism 8 or Origin 2022 (OriginLab). Statistical analysis was performed with in-build functions of GraphPad Prism 8 software as indicated. Normalization was performed to positiv or negative controls as indicated in the figure legends. If not indicated otherwise, plots show mean ±SD values of technical or biological replicates as indicated in the figure legends. Statistical tests applied were also indicated for each data set in the figure legends. Figure illustrations were in parts created with BioRender.com.

Supporting Information

Supporting Information is available from the Wiley Online Library or from the author.

Acknowledgements

A.B. and N.P. contributed equally to this work. The authors thank Robert Drumm, Frano Milos, the INM Imaging Core Facility and Cao Nguyen Doung (Leibniz Institute for New Materials) for help with the bulk rheology measurement, nano-indentation analysis and light microscopy, respectively, and Kathleen Seelert (CIPMM) for help with blood collection and handling. The authors acknowledge funding from the Pharmazeutische Forschungsallianz Saarland, the Daimler and Benz Foundation (32-12/22), the Joachim Herz Foundation (Add-on Fellowship), the DFG (SFB 1027), the Kennedy Trust for Rheumatology Research, UKRI Postdoctoral Fellowship EP/X023907/1, and the Emmy Noether program of the German Science Foundation (project number 525255627).

Open access funding enabled and organized by Projekt DEAL.

Conflict of Interest

The authors declare no conflict of interest.

Data Availability Statement

The data that support the findings of this study are available from the corresponding author upon reasonable request.

Keywords

bottom-up synthetic biology, CD8 Treg, cell mimics, elastomers, immunotherapy, supported lipid bilayers, synthetic cells, synthetic immunology

Received: March 7, 2024
Revised: April 29, 2024
Published online:

[1] A. D. Waldman, J. M. Fritz, M. J. Lenardo, *Nat. Rev. Immunol.* **2020**, *20*, 651.
[2] D. G. M. Tantalo, A. J. Oliver, B. von Scheidt, A. J. Harrison, S. N. Mueller, M. H. Kershaw, C. Y. Slaney, *J. Immuno. Ther. Cancer.* **2021**, *9*, e002555.
[3] D. K. Y. Zhang, K. Adu-Berchie, S. Iyer, Y. Liu, N. Cieri, J. M. Brockman, D. Neuberg, C. J. Wu, D. J. Mooney, *Nat. Commun.* **2023**, *14*, 506.
[4] Y. Li, R. J. Kurlander, *J. Translational Medicine.* **2010**, *8*, 104.
[5] A. Isser, N. K. Livingston, J. P. Schneck, *Biomaterials.* **2021**, *268*, 120584.
[6] G. D. Sckisel, M. N. Bouchlaka, A. M. Monjazeb, M. Crittenden, B. D. Curti, D. E. C. Wilkins, K. A. Alderson, C. M. Sungur, E. Ames, A. Mirsoian, A. Reddy, W. Alexander, A. Soulika, B. R. Blazar, D. L. Longo, R. H. Wiltrout, W. J. Murphy, *Immunity.* **2015**, *43*, 240.
[7] L. H. Lambert, G. K. E. Goebrecht, S. E. De Leo, R. S. O'Connor, S. Nunez-Cruz, T.-D. Li, J. Yuan, M. C. Milone, L. C. Kam, *Nano Lett.* **2017**, *17*, 821.
[8] D. L. Harrison, Y. Fang, J. T.-C. M. Huang, *Frontiers in Physics.* **2019**, *7*, 00045.
[9] E. Judokusumo, E. Tabdanov, S. Kumari, M. L. Dustin, L. C. Kam, *Biophys. J.* **2012**, *102*, L5.
[10] R. S. O'Connor, X. Hao, K. Shen, K. Bashour, T. Akimova, W. W. Hancock, L. C. Kam, M. C. Milone, *J. Immunol.* **2012**, *189*, 1330.
[11] D. J. Yuan, L. Shi, L. C. Kam, *Biomaterials.* **2021**, *273*, 120797.
[12] D. Friedman, P. Simmonds, A. Hale, L. Bere, N. W. Hodson, M. R. H. White, D. M. Davis, *J. Cell Sci.* **2021**, *134*, 258570.
[13] L. E. Jansen, N. P. Birch, J. D. Schiffman, A. J. Crosby, S. R. Peyton, *J. Mech. Behav. Biomed. Mater.* **2015**, *50*, 299.
[14] Q. Qin, D. Wang, L. Xu, Y. Lan, M. Tong, *J. Ultrasound in Medicine.* **2021**, *40*, 1371.
[15] A. Grakoui, S. K. Bromley, C. Sumen, M. M. Davis, A. S. Shaw, P. M. Allen, M. L. Dustin, *Science.* **1999**, *285*, 221.
[16] S. J. Davis, P. A. van der Merwe, *Nat. Immunol.* **2006**, *7*, 803.
[17] M. L. Dustin, *Cancer Immunol. Res.* **2014**, *2*, 1023.
[18] J. E. Hernandez Bücher, O. Staufer, L. Ostertag, U. Mersdorf, I. Platzman, J. P. Spatz, *Biomaterials.* **2022**, *285*, 121522.
[19] H. Jia, P. Schwille, *Curr. Opin. Biotechnol.* **2019**, *60*, 179.
[20] O. Staufer, F. Dietrich, R. Rimal, M. Schröter, S. Fabritz, H. Boehm, S. Singh, M. Möller, I. Platzman, J. P. Spatz, *Sci. Adv.* **2021**, *7*, eabg6666.
[21] O. Staufer, et al., *eLife.* **2021**, *10*, e73556.
[22] E. Jenkins, A. M. Santos, C. O'Brien-Ball, J. H. Felce, M. J. Wilcock, D. Hatherley, M. L. Dustin, S. J. Davis, C. Eggeling, E. Sezgin, *J. Cell Sci.* **2018**, *132*, 219709.
[23] K. Göpfrich, B. Haller, O. Staufer, Y. Dreher, U. Mersdorf, I. Platzman, J. P. Spatz, *ACS Synth. Biol.* **2019**, *8*, 937.
[24] P. F. Céspedes, D. Beckers, M. L. Dustin, E. Sezgin, *FEBS J.* **2020**, *288*, 1070.
[25] O. Staufer, S. Antona, D. Zhang, J. Csatari, M. Schroter, J.-W. Janiesch, S. Fabritz, I. Berger, I. Platzman, J. P. Spatz, *Biomaterials.* **2021**, *264*, 120203.
[26] A. J. Torres, R. L. Contento, S. Gordo, K. W. Wucherpfennig, J. C. Love, *Lab Chip.* **2013**, *13*, 90.
[27] A. H. Lippert, I. B. Dimov, A. K. Winkel, J. Humphrey, J. McColl, K. Y. Chen, A. M. Santos, E. Jenkins, K. Franze, S. J. Davis, D. Klenermam, *Biophys. J.* **2021**, *120*, 35.
[28] M. F. Mescher, *J. Immunol.* **1992**, *149*, 2402 .
[29] O. Campàs, T. Mammoto, S. Hasso, R. A. Sperling, D. O'Connell, A. G. Bischof, R. Mass, D. A. Weitz, L. Mahadevan, D. E. Ingber, *Nat. Methods.* **2014**, *11*, 183.
[30] A. Ohmann, C.-Y. Li, C. Maffeo, K. A. Nahas, K. N. Baumann, K. Gopfrich, J. Yoo, U. F. Keyser, A. Aksimentiev, *Nat. Commun.* **2018**, *9*, 2426.
[31] H. Schuster, J. K. Peper, H.-C. Bosmuller, K. Rohle, L. Backert, T. Bilich, B. Ney, M. W. Loffler, D. J. Kowalewski, N. Trautwein, A. Rabsteyn, T. Engler, S. Braun, S. P. Haen, J. S. Walz, B. Schmid-Horch, S. Y. Brucker, D. Wallwiener, O. Kohlbacher, F. Fend, H.-G. Rammensee, S. Stevanovic, A. Staebler, P. Wagner, *Proc. Natl. Acad. Sci. USA.* **2017**, *114*, E9942.
[32] R. Hammink, J. Weiden, D. Voerman, C. Popelier, L. J. Eggermont, M. Schluck, C. G. Figdor, M. Verdoes, *ACS Appl. Mater. Interfaces.* **2021**, *13*, 16007.
[33] H. Hocheng, C.-M. Chen, Y.-C. Chou, C.-H. Lin, *Microsys. Technol.* **2010**, *16*, 423.
[34] K. Izdihar, H. R. Abdul Razak, N. Supion, M. K. A. Karim, N. H. Osman, M. Norkhairunnisa, *Appl. Sci.* **2021**, *11*, 1172.
[35] A. Knörck, S. Marx, K. S. Friedmann, S. Zophel, L. Lieblang, C. Hassig, I. Muller, J. Pilch, U. Sester, M. Hoth, H. Eichler, M. Sester, E. C. Schwarz, *Transfusion.* **2018**, *58*, 1516.
[36] H. Sudarsanam, R. Buhmann, R. Henschler, *Front. Bioeng. Biotechnol.* **2022**, *10*, 886637.
[37] S. Schwaiger, A. M. Wolf, P. Robatscher, B. Jenewein, B. Grubeck-Loebenstein, *J. Immunol.* **2003**, *170*, 613.
[38] A. Noble, A. Giorgini, J. A. Leggat, *Blood.* **2006**, *107*, 4475.
[39] S. Mishra, S. Srinivasan, C. Ma, N. Zhang, *Front. Immunol.* **2021**, *12*, 708874.
[40] O. Staufer, A. Leithner, S. Zhou, M. Crames, S. Comeau, D. Young, S. Low, E. Jenkins, S. J. Davis, A. Nixon, N. Pefaur, S. Kasturirangan, M. L. Dustin, *bioRxiv.* **2022**, *2015*, 496334.
[41] W. Xu, R. Mezencev, B. Kim, L. Wang, J. McDonald, T. Sulchek, *PLoS One.* **2012**, *7*, e46609.
[42] Y. L. Han, A. F. Pegoraro, H. Li, K. Li, Y. Yuan, G. Xu, Z. Gu, J. Sun, Y. Hao, S. K. Gupta, Y. Li, W. Tang, X. Tang, L. Teng, J. J. Fredberg, M. Guo, *Nat. Phys.* **2020**, *16*, 101.
[43] C.-J. Hsu, W.-T. Hsieh, A. Waldman, F. Clarke, E. S. Huseby, J. K. Burkhardt, T. Baumgart, *PLoS One.* **2012**, *7*, e32398.
[44] L. Flippe, S. Bézie, I. Anegon, C. Guillonneau, *Immunol. Rev.* **2019**, *292*, 209.
[45] S. Park, S. Song, S.-H. Yoon, *Colloids Surf. A.* **2022**, *644*, 128827.
[46] C. Pan, Y. Ohm, J. Wang, M. J. Ford, K. Kumar, S. Kumar, C. Majidi, *ACS Appl. Mater. Interfaces.* **2019**, *11*, 42561.
[47] K. Jiang, P. C. Thomas, S. P. Forry, D. L. DeVoe, S. R. Raghavan, *Soft Matter.* **2012**, *8*, 923.
[48] J. Capera-Aragones, L. Chen, S. Valvo, A. Suri, R. Moniz, M. L. Dustin, *Biophys. J.* **2023**, *122*, 510a.
[49] Z. Xu, C. Shen, Y. Hou, H. Gao, S. Sun, *Chem. Mater.* **2009**, *21*, 1778.

